Journal of Materials Chemistry C

Designing for dopability in semiconducting $AgInTe_2$

Journal:	*Journal of Materials Chemistry C*
Manuscript ID	TC-ART-01-2023-000070.R1
Article Type:	Paper
Date Submitted by the Author:	10-Feb-2023
Complete List of Authors:	Meschke, Vanessa; Colorado School of Mines, Physics Gomes, Lídia; Universidade Federal de Pernambuco, Departamento de Física; University of Illinois, Department of Mechanical Science and Engineering Adamczyk, Jesse; Colorado School of Mines, Physics Ciesielski, Kamil; Colorado School of Mines, Physics Crawford, Caitlin; Colorado School of Mines, Material Science Vinton, Haley; Colorado School of Mines, Mathematics Ertekin, Elif; University of Illinois, Department of Mechanical Science and Engineering Toberer, Eric; Colorado School of Mines,

SCHOLARONE™
Manuscripts

Journal Name

ARTICLE TYPE

Cite this: DOI: 00.0000/xxxxxxxxxx

Designing for dopability in semiconducting $AgInTe_2$[†]

Vanessa Meschke,[a] Lídia Carvalho Gomes[b,c], Jesse M. Adamczyk,[a] Kamil M. Ciesielski[a], Caitlin M. Crawford,[a], Haley Vinton[d], Elif Ertekin[b], and Eric S. Toberer*[a]

Received Date
Accepted Date

DOI: 00.0000/xxxxxxxxxx

Ternary chalcogenide semiconductors (e.g., $CuInTe_2$, $AgInTe_2$, $AgGaTe_2$, Hg_2GeTe_4) have significant potential for excellent thermoelectric performance if appropriately doped. However, the efficacy of extrinsic dopants in these materials varies widely based on their native defect chemistry. Here, we investigate via first principles calculations and experimental transport measurements how native defects populations in $AgInTe_2$ can be synthetically controlled. First principles calculations predict that acceptor V_{Ag}^{1-} vacancies and donor In_{Ag}^{2+} antisite defects are the dominant native defects in $AgInTe_2$. Depending on calculated synthesis conditions, the ratio of these two defect concentrations is predicted to vary by approximately ten orders of magnitude. Experimental transport measurements are correlated with synthetic stoichiometry to assess the predictions of dominant defects and carriers from computation. These results are experimentally tested using two model extrinsic dopants, Zn and Ge. Transport properties of doped samples are considered in regimes where native defects either permit *p*- or *n*-type dopability. Beyond impacting the dopability, the native defect concentrations (V_{Ag} in particular) correlate with significant reduction in thermal conductivity (~0.5 W m^{-1} K^{-1}). Collectively, these results indicate that degenerate *p*- and *n*-type doping of $AgInTe_2$ could be achieved if suitable dopants are identified. In the case of successful *n*-type doping, we expect the lattice thermal conductivity of such samples to be extremely low.

1 Introduction

Multinary tetrahedrally bonded semiconductors (TBS) have often been studied for their photovoltaic[1–3] and thermoelectric[4–7] applications. However, successful applications of these materials have required significant effort to understand the role of native defects and extrinsic dopants and optimize material performance. For example, the undesirable $2V_{Cu}$-V_{Se} vacancy complex in $Cu(In,Ga)Se_2$ (CIGS) leads to metastable properties in devices,[8] but synthesizing in Cu-rich conditions suppresses the formation of these vacancy complexes, thereby improving device performance.[9,10] In other cases, native defects preclude application; for example, Cu_{Zn} in Cu_2ZnSnS_4 (CZTS) are extremely low energy defects even under Cu-poor growth conditions, pinning the Fermi level extremely close to the valence band and limiting solar cell device tunability.[11] As shown by Miller *et al.*, most ternary and quaternary tetrahedrally bonded semiconductors have a fairly narrow range of observed carrier concentrations and often only one available charge carrier type (ie. electron or hole).[12] For example, most Cu-containing TBS present *p*-type in the absence of extrinsic dopants due to V_{Cu} and, to a lesser extent, cation antisite defects (e.g. Cu_{III}).

Considering previous works on Ag-based TBS (Figure 1), we find both carrier types are present but the observed carrier concentration range is narrow for the majority of compounds.[12] Here, bipolar behavior is assumed to have a minimum carrier concentration of 10^{14} cm^{-3}. Complete bipolar dopability would require maximum carrier concentrations of 10^{21} carriers cm^{-3} at room temperature, thus requiring control across approximately fourteen orders of magnitude. The experimentally observed narrow ranges in carrier concentration may arise due to narrow elemental chemical potential windows for tuning defect energetics (and thus narrow phase width) in these compounds. Alternatively, these observed bounds may simply arise from limited resources to explore complex spaces both for native defects and extrinisic dopants. In this work, we focus on $AgInTe_2$ (AIT, Fig. 1 inset) as it has a narrow range of observed carrier concentration and few extrinsic doping efforts to date. Additionally, its chemical simplicity makes it appealing as a model system compared to quaternary analogs.

Undoped AIT has been previously reported with high values of electrical resistivity (~1 – 10 Ωm) and Seebeck coefficient

[a] Physics Department, Colorado School of Mines, Golden, CO 80401
[b] Department of Mechanical Science and Engineering, University of Illinois Urbana Champaign, Champaign, Illinois 61820
[c] Departamento de Física, Universidade Federal de Pernambuco, Cidade Universitária, Recife-PE, Brazil, 50670-901
[d] Mathematics Department, Colorado School of Mines, Golden, CO 80401
† Electronic Supplementary Information (ESI) available. See DOI: 00.0000/00000000.

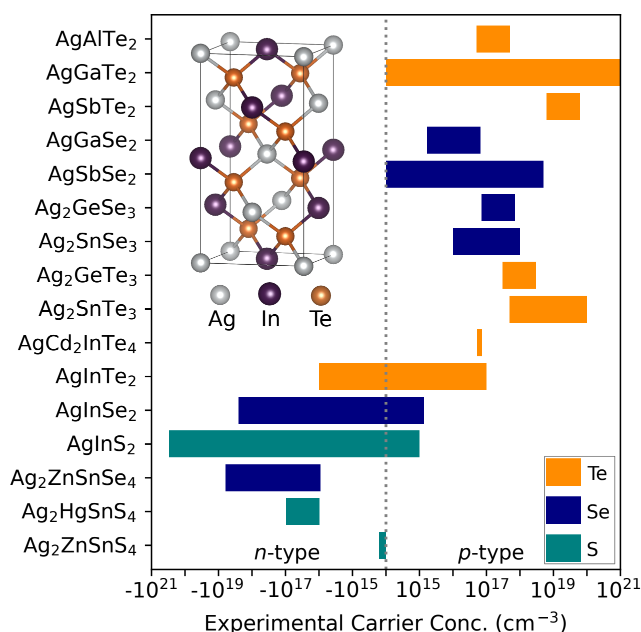

Fig. 1 The experimentally observed carrier concentration of Ag-based tetrahedrally bonded chalcogenides are typically narrow ranges of a singular carrier type. The figure is recreated from data in Ref. 12 and with additional data from Ref. 19. (inset) The chalcopyrite structure of $AgInTe_2$ is the focus of this work.

(+250 – 800 μV/K).[13,14] Hall measurements show low carrier concentration (10^{14} – 10^{17} h^+/cm^{-3}) and significant variation in hole mobility (10–1,000 cm^2 $V^{-1}s^{-1}$).[13,15] Photoconductivity measurements indicate a $\sim$0.95 eV gap.[16,17] *n*-type behavior has been observed for samples annealed under vacuum and sporadically when annealed under a Cd-vapor, though without a consistent trend or mechanistic understanding.[17] To date, first principles defect diagrams have not been reported, though V_{Ag} and In_{Ag} defects are suspected to be dominant in the system, with V_{Te} being cited as another possible defect.[13,17] Keeping in line with other Ag-based TBS, AIT has an inherently low lattice thermal conductivity ($\sim$2 $Wm^{-1}K^{-1}$ at room temperature)[18] that can be lowered by synthesizing in a silver-deficient regime.[13]

In this work, we explore the reported carrier concentration range and assess impact of several extrinsic dopants on AIT. We begin by computationally establishing the elemental chemical potential space for the Ag–In–Te system. Following that, we compare those predictions to experimental determination of the phase diagram surrounding AIT. We then calculate point defect energetics of AIT and associated carrier concentrations; these results are paired with characterization of bulk samples at key points in chemical potential space. Further, these calculations guide the selection of synthetic conditions for effective extrinsic doping. Finally, extrinsic doping with Zn and Ge is pursued experimentally to assess these dopability predictions and the dopability range of AIT with these two elements.

2 Methods

2.1 Experimental Procedure

Polycrystalline samples were prepared using high purity Ag (99.999%, Alpha Aesar), In (99.999%, 5N Plus), and Te (99.999%, 5N Plus) by melt synthesis. Elemental precursors were sealed under vacuum in cleaned fused silica ampules, melted at 1273 K for 5 minutes, quenched in water, and annealed at 573 K for two days. Following the anneal, samples were ground by milling in tungsten carbide ball mill vials for one minute, then ground by hand with an agate mortar and pestle. Following grinding, each sample was passed through a 106 μm mesh sieve, and approximately three grams of sieved powder was loaded into graphite foil–lined graphite dies for pressing. The samples were pressed under vacuum in a house built induction hot press[20] at 723 K for six hours under 40 MPa of pressure, followed by a one hour anneal at 723 K without pressure. The resulting pellets were allowed to cool to room temperature before removing from the press. After pressing, the pellets were removed from the dies and hand-polished to a parallelness within $\pm$ 10μm using a final sandpaper of 2000 grit.

X-ray diffraction (XRD) was performed on the powders using a Bruker D2 Phaser (Cu–Kα radiation) in a θ–2θ configuration for 2θ running from 10° to 100°. Additionally, each pellet was assessed using a FEI Quanta 600i Environmental Scanning Electron Microscope (SEM), and energy dispersive spectroscopy (EDS) was performed on each pellet.

Hall effect and resistivity measurements were performed using the van der Pauw geometry in a house-built instrument from room temperature to 573 K under vacuum using nichrome contacts.[21] Seebeck measurements were performed using a house-built instrument up to 573 K.[22] Repeatability of each measurement for Hall and Seebeck were verified with multi-cycle measurements. Thermal diffusivity was measured using a Netzsch Hyperflash (LFA 467) system on graphite coated samples, and the thermal conductivity was calculated using the Dulong–Petit approximation. The longitudinal and transverse speed of sound were measured using an Olympus 5072PR Pulser/Transceiver unit, and each measurement was repeated three times. The density of each sample was measured geometrically, and the samples were consistently found to be 95% of the theoretical density.

2.2 Computational Procedure

The defect formation energies ΔH(D,q) were calculated from total energies of bulk and defect-containing supercells using density functional theory[23,24] (DFT) as implemented in the Vienna Ab Initio Simulation Package (VASP).[25] The exchange–correction energy functional was approximated by using both the generalized gradient approximation (GGA) of Perdew–Burke–Ernzerhof (PBE)[26] and the Heyd–Scuseria–Ernzerhof (HSE06)[27] hybrid functional, where the hybrid functional defect calculations often show considerable improvement in accuracy for a greater computational cost.

Core and valence electrons were treated with the projector-augmented wave formalism.[28] The Kohn-Sham orbitals were expanded using a plane-wave basis with a cutoff energy of 400 eV.

Lattice parameters and atomic positions were fully relaxed until forces were lower than 1 meV/Å on each atom. For bulk unit cells, the Brillouin zone was sampled using a Γ-centered 4×4×4 k-point grid. Calculations including point defects used a 2×2×2 supercell (64-atom bulk) with a 2×2×2 Γ-centered k-mesh with the HSE06 functional. Unless otherwise stated, all results reported are obtained using the HSE06 hybrid functional.

Due to the presence of the heavy Te elements, spin orbit coupling (SOC) effects were taken into account as shifts applied to the band edges.[29] These were evaluated in a fully relativistic plus hybrid functional calculation. In the presence of SOC, a shift of the valence band maximum of 0.22 eV upwards in energy reduces the band gap from 0.9 eV (as evaluated using the HSE06 hybrid functional) to 0.71 eV. Band edge positions used to plot the defect diagrams were then adjusted according to the HSE06 + SOC calculations.

Using the supercell approach, the formation energy ΔH of a point defect D with charge q is computed as:[30]

$$\Delta H(D,q) = E(D,q) - E(H) - \sum_i n_i \mu_i + qE_F + E_{corr} \quad (1)$$

where E(D,q) and E(H) are the total energy of the defect-containing and host supercells, respectively. n_i is the number of atoms of species i with chemical potential μ_i added ($n_i > 0$) or removed ($n_i < 0$) from the supercell to create the defect. E_F is the Fermi level, which ranges from the valence band maximum to the conduction band minimum, and E_{corr} is a correction term used to account for finite size effects. To calculate E_{corr}, the approach used by Lany and Zunger[31] was used to calculate the potential alignment correction ($\Delta E_{pa} = q\Delta V_{pa}$) and the image charge correction ($\Delta E_i = q^2 \alpha_M / 2\varepsilon\omega^{-1/3}$). The chemical potential describes the energy of reservoirs with which atoms in the system are being exchanged. For a compound in thermodynamic equilibrium, the chemical potential is the sum of the number of atoms of type i in the composition times the chemical potential of species i ($\mu_{comp.} = \sum_i n_i \mu_i$). For $AgInTe_2$, the chemical potential is written as:

$$\mu_{AgInTe_2} = \mu_{Ag} + \mu_{In} + 2\mu_{Te} \quad (2)$$

By referencing the chemical potentials to the bulk elemental phases (μ^o), the above equation is instead written as:

$$\mu_{AgInTe_2} = (\mu^o_{Ag} + \Delta\mu_{Ag}) + (\mu^o_{In} + \Delta\mu_{In}) + 2(\mu^o_{Te} + \Delta\mu_{Te}) \quad (3)$$

As shown in previous works,[32–34] using the results of first principles calculations in conjunction Eqn. 1 is an effective approach for understanding defects in the context of experimental synthesis conditions. Here, we assume that defect concentrations are "locked in" at the synthesis temperature and cannot equilibrate to measurement temperature, whereas electron and hole carriers can and do equilibrate. Following this assumption, the formation energies calculated with Eqn. 1 can be related to concentration by:

$$\left[D_q\right] = N_X \exp\left[\frac{-\Delta H(D,q)}{k_b T_S}\right] \quad (4)$$

where $\left[D_q\right]$ is the concentration of defect D in charge state q, N_X is the concentration of sites the defect can impact in cm^{-3}, k_b is the Boltzmann constant, and T_S is the synthesis temperature (723 K). To utilize Eq. 4, the equilibrium Fermi level is required, as ΔH(D,q) depends on E_F for charged defects. The equilibrium Fermi level must satisfy the charge neutrality condition:

$$\sum_D q\left[D_q\right] - n + p = 0 \quad (5)$$

where the electron (n) and hole (p) concentrations are approximated through a single parabolic band (SPB) model as:

$$n = 2\left(\frac{2\pi m_e^* k_b T}{h^2}\right)^{3/2} \exp\left[\frac{E_f - E_{CBM}}{k_b T}\right] \quad (6)$$

$$p = 2\left(\frac{2\pi m_h^* k_b T}{h^2}\right)^{3/2} \exp\left[\frac{E_{VBM} - E_f}{k_b T}\right] \quad (7)$$

where m_e^* and m_h^* are the density of states effective masses of the electrons and holes, respectively, h is Planck's constant, E_F is the position of the Fermi level, and E_{VBM} and E_{CBM} are the energies of the extrema of the valence and conduction bands, respectively. When using Eqns. 6 and 7 in determining charge neutrality to calculate defect concentrations, the synthesis temperature is used. To determine the free carrier concentration at any desired measurement temperature, the defect concentrations are kept constant and the Fermi level is recalculated using Eqns. 5, 6, and 7. In the latter two equations, the temperature now refers to the measurement, rather than synthesis, temperature.

3 Results

We begin by examining the Ag–In–Te chemical potential and composition spaces through a combination of first principles calculations and experiment. Computation predicts $AgInTe_2$ is a member of seven distinct three-phase regions, and experiment confirms the existence of the majority of these regions. After determining the experimental phase diagram, the native defects across the space are assessed to establish the most likely regions of n- and p-type dopability. Extrinsic dopants are introduced to these regions, and bulk samples of doped and undoped $AgInTe_2$ are characterized for their electronic and thermal properties.

3.1 Phase Stability of $AgInTe_2$ in Chemical Potential Space

A critical step in calculating defect formation energies in a compound is calculating the bounds of the elemental chemical potentials that define the range of the compound's stability. The compound's extent in chemical potential space determines the limits for achievable defect concentrations in the system, as shown in Eqn. 1. The bounding points in chemical potential space can be directly correlated to regions of composition space; for a ternary system, these points correspond to three phase regions.[35] For AIT, first principles calculations predict seven invariant points where AIT forms three phase equilibria with competing compounds. These points are labeled AI1, AI2, ..., AT3 and are shown in the 3-dimensional chemical potential space map in Figure 2. The notation for each invariant point was selected to denote which two elements (A: Ag, I: In, T:Te) are in excess at said point.

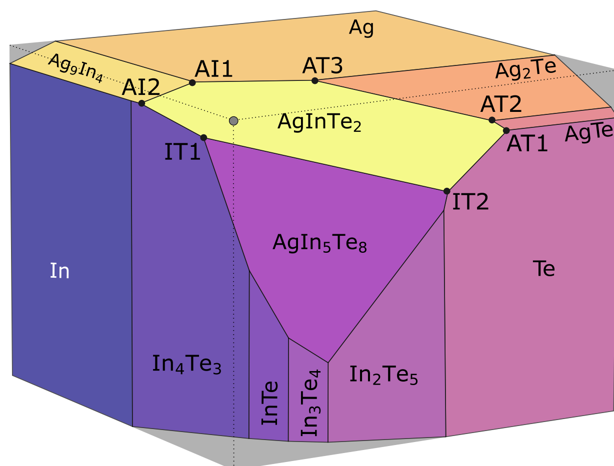

Fig. 2 $AgInTe_2$ (yellow) lives within the Ag-In-Te elemental chemical potential space. The grey circle indicates the point where elemental Ag, In, and Te are in equilibrium (i.e., $\Delta\mu_{Ag} = \Delta\mu_{In} = \Delta\mu_{Te} = 0$ eV/atom). Binary and ternary compounds that are more stable than the constituent elements appear as bevels to the cube. There are seven invariant points involving $AgInTe_2$; at each invariant point three phases are in equilibrium. The label at each invariant point indicates which two elements are in excess (A: Ag, I: In, T: Te). For each element, the $\Delta\mu$ range considered is from 0 to -2 eV/atom.

In Figure 2, the chemical potentials of compounds are described as equations of planes following the format $n_{Ag}\Delta\mu_{Ag}$ + $n_{In}\Delta\mu_{In}$ + $n_{Te}\Delta\mu_{Te}$ - ΔH = 0. Elemental Ag, In, and Te are planes where each corresponding chemical potential is 0 ($\Delta\mu_{Ag} = 0$, $\Delta\mu_{In} = 0$, and $\Delta\mu_{Te} = 0$), which can be visualized as three orthogonal planes that create a square box. Additional planes are cut away from the box where compounds are more stable than the elemental solids. Of most interest in this space are points where three planes, one of which is for $AgInTe_2$, intersect, labelled AI1, AI2, *etc.*. These correspond to three-phase equilibria that pin chemical potentials, and can be used to determine defect formation energies. Considering all seven three-phase regions present in the system bordering AIT, the chemical potential limits for each element within AIT are -0.58 eV $\leq \Delta\mu_{Ag} \leq$ 0 eV, -1.4 eV $\leq \Delta\mu_{In} \leq$ -0.09 eV, and -0.75 eV $\leq \Delta\mu_{Te} \leq$ 0 eV. A list of all equilibrium chemical potential points named in this work is included in Supplement Table S3. The extent of the bounding chemical potentials determines the amount of variation in defect energetics that are achievable for a compound. Compared to $CuInTe_2$,[32] AIT has a very similar extent in chemical potential space, predicting similar variations in defect energetics. This is not to say, however, that the absolute magnitude of the defect formation energies are necessarily similar.

To assess the accuracy of the predicted chemical potential space, we compare Figure 2 with the experimentally observable phase space (Figure 3). Bulk samples were synthesized near the nominal stoichiometry of $AgInTe_2$ and studied with XRD, SEM, and EDS. Details of the findings from XRD are included in the supplemental, as are micrographs from SEM and summaries of EDS. Figure 3 shows the phase diagram surrounding $AgInTe_2$. Of the seven computationally predicted three-phase regions, four show good agreement with experimental characterization with SEM and EDS (IT2, AT1, AT2, and AT3). The remaining regions show slight differences between the computational and experimental phase diagrams that likely arise from uncertainties introduced by DFT due to the method used to compute formation energies. Typical uncertainties for these types of calculations are around 0.05 - 0.1 eV per atom,[36] and our calculations fall within this uncertainty. The effects of these inaccuracies are shown in the AI2 and IT1 regions, both of which experimentally contained the compound InTe instead of the predicted In_4Te_3, and the AI1 and AI2 regions, which form with Ag_3In instead of Ag_9In_4. Since Ag_3In was not predicted to be stable by computation, it does not appear in the chemical potential map. These inaccuracies are not unexpected for such a complex phase space; theory only failed to accurately predict equilibria in regions with tight tolerances on $\Delta\mu$ values. Considering Figure 2, increasing the stability of the InTe phase by 100 meV per formula unit is sufficient to recover the appropriate phase diagram in this region. Similarly, increasing the stability of Ag_3In by 150 meV per formula unit recovers the experimentally observed phases. Such a change does not radically shift the positions of AI2 and IT1 in chemical potential space. Additionally, $AgIn_5Te_8$ was difficult to observe as a distinct phase from $AgInTe_2$ due to the similar chemistry and structural parameters. However, phases containing $AgIn_5Te_8$ show broader peaks in XRD, likely due to a solid solution forming between the two compounds.

In conclusion, $AgInTe_2$ is experimentally found to form seven three-phase regions with elemental Ag and Te, the binary compounds Ag_3In, InTe, AgTe, and Ag_2Te, and the ternary compound $AgIn_5Te_8$. While the experimentally observed and the computationally predicted chemical potential spaces do not perfectly match, the calculated defect formation energies can still be useful in understanding the behavior of AIT in different synthetic conditions. Having developed an understanding of the phase equilibria of $AgInTe_2$, we move to studying the native defects in $AgInTe_2$ and the limits on the achievable carrier concentration those defects impose.

3.2 Native Defects

The defect concentrations across the extrema of the AIT chemical potential space are calculated using Eqn. 4. The full defect diagrams for all predicted chemical potential points are included in the supplemental (Figure S24). Since the chemical potential space for AIT is rather complex, a Brouwer band diagram (Figure 4) is presented to more efficiently compare the concentrations of defects around the perimeter of the equilibrium chemical potential space. For AIT, the highest concentration defects are V_{Ag}^{-1} and In_{Ag}^{+2} for most invariant points. In-deficient conditions (AT1, AT2, and AT3) are the exception to this trend, where Ag_{In} defects become more common than In_{Ag}^{+2}. The total concentration of defects spans two orders of magnitude between the invariant points and are highest at IT1 and IT2 ($\sim 10^{19}$ cm^{-3}), while AT1, AT2, and AT3 show the lowest defect concentrations ($\sim 10^{17}$ cm^{-3}). For all invariant points, indium and tellurium vacancies have high formation energies, and thus low concentrations, and do not impact material properties greatly. The energetics presented here

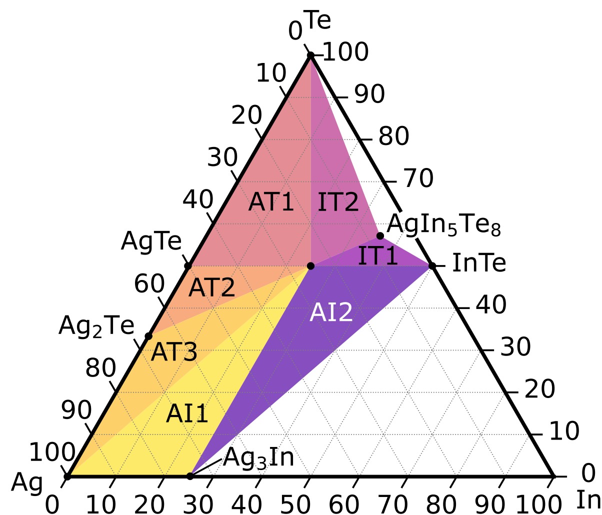

Fig. 3 Bulk synthesis of samples near the $AgInTe_2$ composition at 723 K yield seven three-phase regions. Only regions in equilibrium with $AgInTe_2$ are shown. Each three-phase region is labeled to denote which two elements are in excess (A: Ag, I: In, T: Te). The AI1, AI2, and IT1 regions are found to be slightly different than computationally predicted (Figure 2).

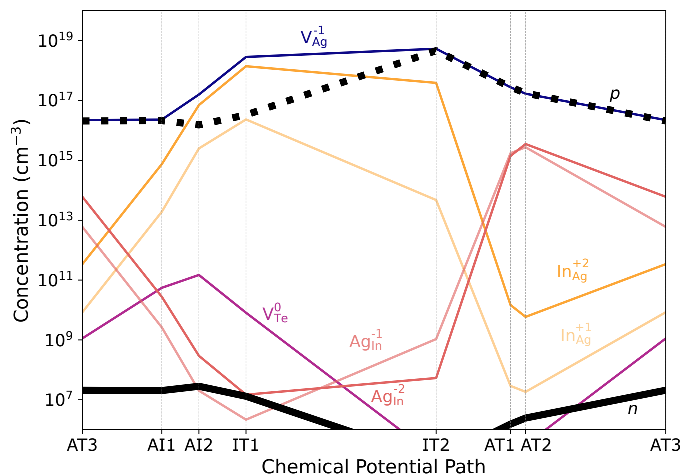

Fig. 4 The calculated Brouwer defect diagram shows how the elemental chemical potentials change the concentration of defects in $AgInTe_2$. The system is predicted to be p-type regardless of elemental chemical potentials due to the high concentration of acceptor V_{Ag} defects. Defect concentrations are set at a synthesis temperature of 723 K while the carrier concentrations (n and p) are calculated assuming measurement at 300 K.

run contrary to previous experimental works[13,37] that claimed tellurium vacancies have a pronounced effect on AIT's electrical properties.

The Brouwer band diagram additionally plots the electron (n) and hole (p) concentrations across the boundary of the AIT chemical potential space. As part of determining overall charge neutrality (Eqn. 5), we predict the electron and hole concentrations (Figure 4) at 300K. Throughout chemical potential space, AIT is predicted to be natively p-type with hole concentrations (10^{16}-10^{18} cm^{-3}) low compared to an optimized thermoelectric material ($\sim 10^{19}$ cm^{-3}). The predicted hole concentration is the highest where the acceptor V_{Ag}^{-1} has the highest concentration and is not compensated by donor In_{Ag} defects, which occurs at points IT1 and IT2.

The electron concentration is predicted to be low ($< 10^7$ e$^-$/cm^3) throughout the space at 300K. However, by 723 K, charge neutrality indicates p is only two orders of magnitude larger than n (Supplemental Figure S25). Likewise, the equilibrium Fermi level at 300K is 0.39 eV for AI2; this is quite close to the bipolar transition energy (E_F where $n = p$) of 0.44 eV. These energetic differences are within the uncertainty of defect calculations and suggests that bipolar behavior may be possible in some undoped AIT samples.

3.3 n- and p-Type Dopability Window

Beyond describing which defects are the most energetically favorable in a system, defect diagrams provide insight into how native defects limit the dopability of a material. On a defect diagram, the "dopability window" is the formation energy of the lowest energy defect at the valence band (for p-type dopability) or conduction band (n-type dopability). More positive values of the dopability window indicate more potential for dopability, while more negative values indicate the native defects in a material will hinder the dopability. To illustrate this behavior, we consider two specific chemical potential points, namely, AI2 and IT2. In the AI2 region (Figure 5a), the high chemical potential of Ag increases the formation energy of V_{Ag} and yields a positive energy at the conduction band (denoted with a black arrow) and thus an n-type dopability window. At the valence band, In_{Ag} antisite defects have a low formation energy that would prevent the Fermi level from moving within 0.1 eV from the valence band. In_{Ag} as such acts as a 'killer defect' that intrinsically limits the p-type dopability at point AI2. Considering the IT2 region (Figure 5b), a very large p-type dopability window is enabled by the increase in In_{Ag} energy; however, the n-type dopability is severely restricted by V_{Ag}.

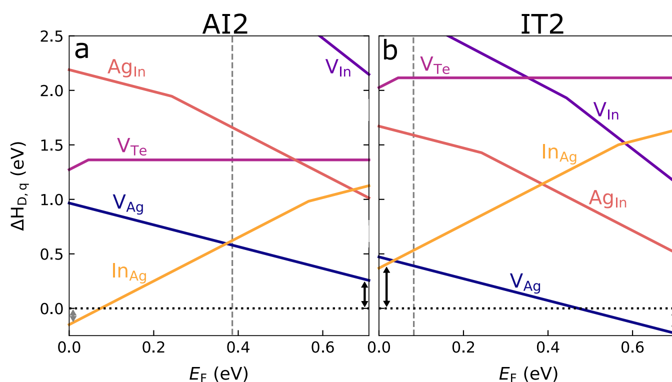

Fig. 5 (a) V_{Ag} and In_{Ag} defects are calculated to have similar formation energies at point AI2, leading to intrinsic behavior. (b) At point IT2 the formation energy of V_{Ag} decreases and the hole concentration correspondingly rises. AI2 shows an n-type dopability window, as shown by the black arrow on the right, but not a p-type dopability window, as shown by the grey arrow on the left. The opposite is true for IT2. Equilibrium positions of the Fermi level are denoted by the vertical grey dashed lines.

The dopability windows around the perimeter of AIT's chemical potential space are shown in the Brouwer dopability diagram in Figure 6. In AIT, regions AI1, AI2, and AT3 have *n*-type dopability windows, while regions AI1, IT2, AT1, AT2, AT3 have *p*-type dopability windows with no defects severely limiting the dopability. For regions with negative dopability windows (AI2, IT1, IT2, AT1, and AT2), three main defects are responsible. Negative *n*-type dopability windows are set by either V_{Ag} or In_{Ag} depending on which element is in excess. When In is in excess, the increase in $\Delta\mu_{In}$ increases the formation energy of Ag_{In}, which causes V_{Ag} to dominate. For the negative *p*-type dopability windows, Ag_{In} exclusively determines the height since few other defects are low energy at the VBM. To assess the specifics of each dopability window, the full defect diagrams should be examined (see Supplemental Figure S24). As discussed above, region AI2 is particularly useful to explore for *n*-type dopability given the presence of an *n*-type dopability and lack of *p*-type, while region IT2 would be favorable for *p*-type doping for the opposite reason; these two regions are the focus of the experimental efforts henceforth.

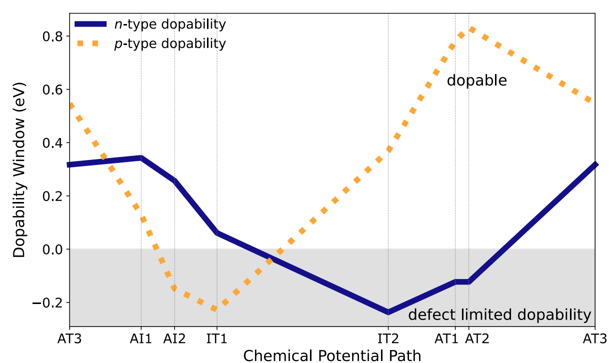

Fig. 6 The available *n*- and *p*-type dopability windows depend strongly on the elemental chemical potentials. Negative dopability windows, highlighted by the grey section of the plot, indicate regions where dopability is limited by the native defects in the system (i.e., V_{Ag} and In_{Ag}).

3.4 Synthesis and Undoped Electronic Properties

To assess the dopability predictions discussed above, samples were prepared at the AI2 and IT2 invariant points. While invariant point AI2 showed discrepancy from the predicted phase equilibria, this point showed the most promise for assessing *n*-type dopability, as discussed above. AI2 samples were prepared with a nominal stoichiometry of $AgInTe_{1.96}$, which contained small amounts of impurity phases Ag_3In and InTe. IT2 samples were prepared with a nominal stoichiometry of $Ag_{0.98}InTe_2$, which contained small amounts of impurity phases $AgIn_5Te_8$ and Te. These hot pressed samples had densities >95% and the desired secondary phases between 2% – 13% by Rietveld refinement (Sup. Figures S4 and S8). While impurity phases can greatly impact materials properties, we do not expect the 13% impurity phase observed for point IT2 to greatly impact charge transport in this sample. $AgIn_5Te_8$ characterized in our lab was extremely resistive, with a carrier concentration on the order of 10^{13} cm^{-3} and electrical resistivity of 10^6 mΩ-cm. Additionally, our measurements in region IT2 show good agreement with previously reported electronic properties for samples of similar compositions.[13]

Electrical resistivity, Hall, and Seebeck measurements were conducted between 50-300°C. For invariant point IT2, theory predicted a carrier concentration on the order of 10^{18} h^+ cm^{-3} at 323 K. Experimental measurements show an average hole concentration of 10^{18} h^+ cm^{-3} and a resistivity of 10^4 mΩ-cm (Figure 7a). On the other hand, invariant point AI2 is predicted to be nearly bipolar (Figure 5) with a hole concentrations of $\sim10^{16}$ per cm^3 at 323 K. Experimental Hall effect measurements show *n* type behavior, with a measured electron concentration of $\sim10^{13}$ cm^{-3} and resistivity of 10^7 mΩ-cm Figure 7a). Given that the Hall data for AI2 is likely compensated, the exact value should be treated as approximate. AI2 shows the expected compensated Seebeck coefficient of a bipolar material with a small, negative Hall carrier concentration and high resistivity (Figure 7b).

In summary, we show the predictions from defect calculations match experimental observations remarkably well. Despite the discrepancies between the predicted and observed phase diagram for point AI2, theory and experiment agree that this is a highly resistive sample. In contrast, point IT2 experimentally shows a relatively high carrier concentration for the AIT system, as was predicted from computation. This behavior is matched by the relatively low, positive Seebeck coefficient.

3.5 Single parabolic band approximation analysis

For samples with a dominant carrier type (i.e., IT2), single parabolic band analysis provides an opportunity to compare theory- and experiment-derived effective mass and Fermi level values. Recalling the electronic data, point IT2 had a predicted carrier concentration of 10^{18} holes/cm^3 at room temperature. Experimental measurements agreed well with prediction, showing a resistivity of 10^4 mΩ-cm, a *p*-type carrier concentration on the order of 10^{18} cm^{-3}, and a mobility of $\sim$10 cm^2/V·s at room temperature. The Seebeck coefficient was approximately 250 μV/K at room temperature, a fairly reasonable value for this sample's carrier concentration. Assuming acoustic phonon scattering, the effective mass of this sample was calculated as 0.32 m_e at room temperature. Compared to the m^*_{DOS} of 0.426 m_e for holes calculated from first principles, theory and experiment show good agreement here. Additionally, theory predicts the effective masses of holes are approximately 20 times heavier than that of the electrons (m^*_h = 0.426 and m^*_e = 0.016) so the Hall and Seebeck's sign transition will not actually occur at the point when $n \approx p$.

3.6 Extrinsic dopants

To experimentally evaluate the predictions of extrinsic dopability suggested by the native defect analysis above, Ge and Zn were added as model extrinsic dopants to samples in the AI2 and IT2 regions. We focused our doping efforts on the cationic sites since doping the Te site proved more challenging in our experiments. Additions of Sb and Br to $AgInTe_2$ resulted in cracked ampules when melting and highly porous samples. In the follow-

ing section, we will first discuss possible dopants for a I-III-VI_2 system. Following dopant selection, we outline the possible sites for dopants to occupy and the resulting effects on transport. Finally, we examine the experimental transport data of the doped samples in regions AI2 and IT2 and assess the dopability predictions.

To select dopants, we used standard charge counting for a I–III–VI_2 TBS. To dope these materials *n*-type, either a Group II or Group IV element can act as a donor depending on the site occupied (II_I or IV_{III}). However, a Group II dopant may also reside on II_{III} as an acceptor and self-compensate. Achieving *p*-type doping with cations is more challenging; while a II_{III} substitution is desirable in this case, self-compensation may occur if the II_I also forms. While I_{III} could also be considered for *p*-type doping, it is more likely that the dopant would occupy the Group I site and produce no effect. This analysis suggests cation-based *p*-type doping in $AgInTe_2$ will be challenging given the ability for a Group II element to occupy either the Ag or In site and self-compensate.

Given these constraints, we selected Zn (Group II) and Ge (Group IV) to test the *n*- and *p*-type dopability predictions. Ge was selected as the *n*-type dopant as it will likely occupy the In site and produce donor Ge_{In}^{1+} defects. Similarly, Zn was selected as the Group II dopant, which could act as either an acceptor (Zn_{In}^{1-}) or donor (Zn_{Ag}^{1+}) dopant, depending on site occupation. In the following section, we consider two regions to test these dopants: AI2, which was predicted to have generous *n*-type dopability, and IT2, which was predicted to have *p*-type dopability. The doped samples have 0.02 formula units of dopants included in the nominal stoichiometry (e.g., AI2 + $Ge_{0.02}$: $AgInTe_{1.96}Ge_{0.02}$).

First examining region AI2, a silver and indium rich region of chemical potential space, we recall that the undoped sample had a low, *n*-type carrier concentration (10^{13} e^-/cm^3) and low, negative Seebeck coefficient (~-100μV/K) with the hallmarks of a sample with bipolar conduction. Doping with Ge increased the carrier concentration to 10^{15} e^-/cm^3 and decreased the electrical resistivity by an order of magnitude at room temperature (Figure 7a). The Seebeck coefficient shows little change when Ge is added. The modest increase in carrier concentration does not necessarily mean that only 10^{15} Ge_{In} cm^{-3} were incorporated into the lattice. Rather, examination of Figure 5 suggests that the formation energy of V_{Ag} will decrease commensurately in concentration with Ge_{In}, largely nullifying effects of the increase in Ge concentration until the Fermi level is close to the conduction band edge.

The addition of Zn to AI2 resulted in similar effects to doping with Ge, but with more pronounced effects on electronic properties. Experimental Hall measurements report a carrier concentration of approximately 10^{16} e^-/cm^3 and showed the electrical resistivity decrease by two orders of magnitude at room temperature. This suggests Zn has a slightly higher solubility than Ge at the AI2 point and is selectively occupying the Ag site, despite being at a point that is nominally Ag 'rich'. Interestingly, the Seebeck coefficient shows a delayed roll over compared to other samples in region AI2, suggesting Zn has pushed the sample further towards a single band regime than Ge. In summary, both Ge and Zn acted as *n*-type dopants by preferentially occupying the In and Ag sites, respectively.

Region IT2 shows the potential for significant *p*-type dopability and limited *n*-type dopability given the formation energies of In_{Ag} and V_{Ag}, respectively (Figure 5b). Recall the undoped sample showed a measured carrier concentration of 10^{18} h^+/cm^3 and resistivity of 10^4 mΩ-cm. Beginning with Ge, we expect Ge_{In} defects to dominate and serve as a compensating donors that lower the hole concentration. Indeed, the addition of Ge decreases the carrier concentration to 10^{13} h^+/cm^{-3} and increases the electrical resistivity by 2 orders of magnitude (Figure 7a). Consistent with these observations, the Seebeck coefficient also increases to greater than 1,000 μV/K at room temperature (Figure 7 b). Similarly to Ge, doping with Zn decreases the carrier concentration to 10^{12} h^+/cm^{-3} and increases both the resistivity and Seebeck coefficient, suggesting Zn is partially compensating the native defect V_{Ag}. While Zn could be an ambipolar dopant, sitting on either the Ag or In site, it appears to favor the Ag site. Given the high concentration of V_{Ag} at point IT2, this result is unsurprising. Similar results were noted in the indium deficient region AT1 (see Supplemental Figure S26), suggesting Zn_{In} defects are relatively high in energy compared to Zn_{Ag}. In summary, the additions of Ge and Zn pushed IT2 toward an *n*-type regime, but ultimately did not reach solely *n*-type conduction. Given the low formation energy of V_{Ag} that sets the -0.2 eV *n*-type dopability window, this result is unsurprising. Because of this 'killer defect', we do not expect to find strong *n*-type performance at point IT2; the V_{Ag} will stop the Fermi level from moving much beyond mid-gap. Our results do not preclude *p*-type dopability in region IT2; rather, it shows the challenges of finding a suitable *p*-type dopant.

3.7 Thermal Conductivity

To assess if the defect concentrations induced significant changes in thermal transport, laser flash diffusivity measurements were conducted to high temperature. The electronic component of the total thermal conductivity is effectively null for all samples measured due to the high electrical resistivity, thus the total lattice thermal conductivity is approximately equal to the lattice contribution alone (Figure 8). For most samples in both AI2 and IT2 regions, room temperature measurements of lattice thermal conductivity are less than 2 $Wm^{-1}K^{-1}$ and decrease with temperature, approximately matching predicted values from DFT.[38] In all samples, some decay in lattice thermal conductivity with increasing temperature is found and attributed to phonon-phonon scattering.[39]

The undoped AI2 sample shows significantly higher values of thermal conductivity at all temperatures compared to IT2. Considering Figure 4, IT2 has high concentrations of V_{Ag} (10^{19} cm^{-3}) whereas AI2's defects are predominately a mix of V_{Ag} and In_{Ag} in nearly equal concentrations (10^{16} cm^{-3}). At AI2, vacancies are predicted to be approximately two orders of magnitude lower than at IT2. Thus, we expect AI2 to be primarily limited by phonon-phonon scattering whereas IT2 has phonon-phonon and defect-phonon scattering rates that are quite similar in magnitude.

For the extrinsic dopants Ge and Zn, doping in the AI2 region

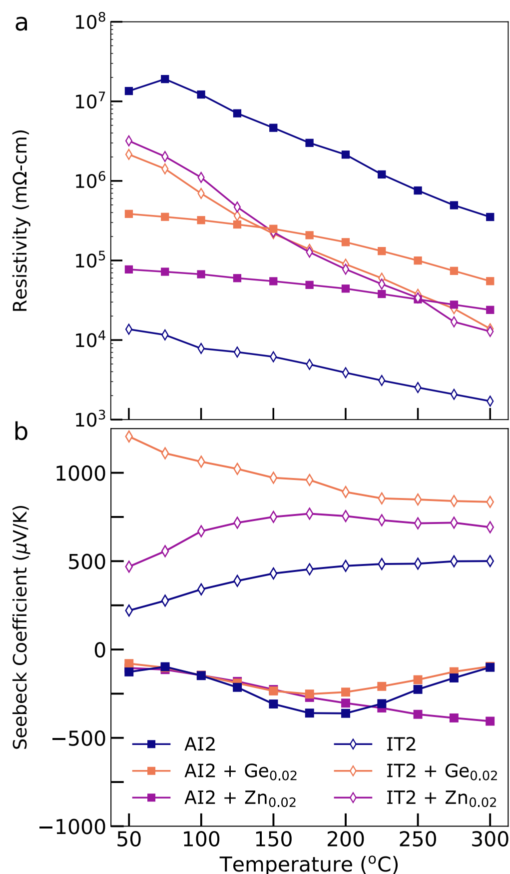

Fig. 7 High-temperature (a) resistivity and (b) Seebeck measurements of undoped and doped AIT consistently show non-degenerate and bipolar behavior. Zn- and Ge-doped samples act as donors in both regions AI2 (filled squares) and IT2 (empty diamonds).

significantly lowers the thermal conductivity to values near IT2. In both cases, the mass contrast of the antisite defects (Zn_{Ag}, Ge_{In}) is quite strong and will scatter phonons. Further, both defects move the Fermi level towards the conduction band. As shown in Figure 5, this shift will increase the concentration of V_{Ag}. IT2 shows a small increase in thermal conductivity with the incorporation of extrinsic dopants. This is somewhat surprising as the Fermi level shift from Ge and Zn doping once again should lower the energy of V_{Ag}.

Comparing AIT to other Ag-containing TBS, we find this system to have typical values of lattice thermal conductivity.[13,18] However, AIT has a much lower lattice thermal conductivity than its Cu analog, $CuInTe_2$ (CIT).[32] Where AIT shows thermal conductivity less than 2 $Wm^{-1}K^{-1}$ regardless of synthetic conditions pursued here, CIT shows thermal conductivity ranging from 2 - 5.5 $Wm^{-1}K^{-1}$.[32] Previous works have stated that the root cause of the low thermal conductivity of Ag-containing TBS is local distortions around the Ag atoms arising from relatively weak bonding with Te.[40,41] The argument for the Ag-Te bond being weaker than the Cu-Te bond is confirmed in measurements of the speed of sound, which averaged ∼3000 m/s for longitudinal and ∼1500 m/s for shear speed of sound for AIT (Supplemental Table S1). In contrast, CIT has been reported to have an average longitudinal speed of sound of ∼3500 m/s and shear speed of sound of ∼1800 m/s.[32,42,43] While the argument for weak bonding leading to local distortions that scattering phonons is intriguing, variations in defect concentrations between these compounds may also play a significant role in their differences in lattice thermal conductivity.

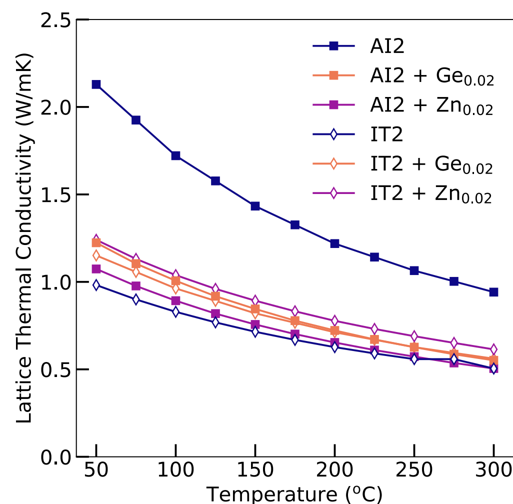

Fig. 8 High-temperature measurements of lattice thermal conductivity show consistently low values at high temperature. The notable exception is the most p-type sample, undoped AI2, possibly due to a lower concentration of V_{Ag}.

4 Conclusions

Developing complex semiconductors for electronic applications requires design strategies to control and harness native defects. In this work, we predicted that $AgInTe_2$ is extremely sensitive to growth conditions for both *p*- and *n*-type dopability. Specifically, we predicted that *n*-type dopability is optimized under Ag-rich conditions and *p*-type doping is optimized under In-poor conditions. These dopant calculations were validated experimentally through the synthesis and characterization of bulk, polycrystalline samples. The dependence of free carrier concentration on synthetic conditions was consistent with our theoretical calculations. As model dopants, Zn and Ge were found to primarily serve as donors in $AgInTe_2$, presumably through Zn_{Ag} and Ge_{In} substitutional defects. Further, both doped and undoped samples with high concentrations of V_{Ag} defects exhibited strongly suppressed thermal conductivity. As such, this study highlights the potential for $AgInTe_2$ as a thermoelectric material if appropriate extrinsic dopants for *n*-type transport can be identified.

Conflicts of interest

There are no conflicts to declare.

Acknowledgements

V. Meschke acknowledges support by the National Science Foundation (NSF) Graduate Research Fellowship Program under Grant No. 1646713. Additional support from the NSF via grants DMR1729594 and DMR1729149 are acknowledged for all other authors. This research is part of the Blue Waters sustained-petascale computing project, which is supported by the National

Science Foundation (awards OCI-0725070 and ACI-1238993) the State of Illinois, and as of December, 2019, the National Geospatial-Intelligence Agency. Blue Waters is a joint effort of the University of Illinois at Urbana-Champaign and its National Center for Supercomputing Applications.

Notes and references

1 D. Shin, B. Saparov and D. B. Mitzi, Advanced Energy Materials, 2017, **7**, 1602366.
2 J. Britt and C. Ferekides, Applied physics letters, 1993, **62**, 2851–2852.
3 D. Jenny, J. Loferski and P. Rappaport, Physical Review, 1956, **101**, 1208.
4 A. Yusufu, K. Kurosaki, A. Kosuga, T. Sugahara, Y. Ohishi, H. Muta and S. Yamanaka, Applied Physics Letters, 2011, **99**, 061902.
5 R. Liu, L. Xi, H. Liu, X. Shi, W. Zhang and L. Chen, Chemical Communications, 2012, **48**, 3818–3820.
6 B. R. Pamplin, T. Kiyosawa and K. Masumoto, Progress in Crystal Growth and Characterization, 1979, **1**, 331–387.
7 M. Telkes, American Mineralogist: Journal of Earth and Planetary Materials, 1950, **35**, 536–555.
8 L. Kerr, S. S. Li, S. Johnston, T. Anderson, O. Crisalle, W. Kim, J. Abushama and R. Noufi, Solid-State Electronics, 2004, **48**, 1579–1586.
9 S. Lany and A. Zunger, Journal of Applied Physics, 2006, **100**, 113725.
10 M. Igalson, P. Zabierowski, D. Prządo, A. Urbaniak, M. Edoff and W. N. Shafarman, Solar Energy Materials and Solar Cells, 2009, **93**, 1290–1295.
11 S. Chen, X. G. Gong, A. Walsh and S.-H. Wei, Applied Physics Letters, 2010, **96**, 021902.
12 S. A. Miller, M. Dylla, S. Anand, K. Gordiz, G. J. Snyder and E. S. Toberer, npj Computational Materials, 2018, **4**, 71.
13 Y. Zhong, Y. Luo, X. Li and J. Cui, Scientific Reports, 2019, **9**, 18879.
14 Y. Aikebaier, K. Kurosaki, T. Sugahara, Y. Ohishi, H. Muta and S. Yamanaka, Materials Science and Engineering: B, 2012, **177**, 999 – 1002.
15 A. Singh and R. Bedi, Thin Solid Films, 2001, **398-399**, 427–431.
16 C. Bellabarba, J. Ganzáles, C. Rincón and M. Quintero, Solid State Communications, 1986, **58**, 243–246.
17 B. Tell, J. L. Shay and H. M. Kasper, Physical Review B, 1974, **9**, 5203–5208.
18 A. Charoenphakdee, K. Kurosaki, H. Muta, M. Uno and S. Yamanaka, Materials Transactions, 2009, **50**, 1603–1606.
19 S. N. Guin, A. Chatterjee, D. S. Negi, R. Datta and K. Biswas, Energy & Environmental Science, 2013, **6**, 2603–2608.
20 A. D. LaLonde, T. Ikeda and G. J. Snyder, Review of Scientific Instruments, 2011, **82**, 025104.
21 C. Wood, A. Lockwood, A. Chmielewski, J. Parker and A. Zoltan, Review of Scientific Instruments, 1984, **55**, 110–113.
22 S. Iwanaga, E. S. Toberer, A. LaLonde and G. J. Snyder, Review of Scientific Instruments, 2011, **82**, 063905.
23 P. Hohenberg and W. Kohn, Physical Review, 1964, **136**, B864–B871.
24 W. Kohn and L. J. Sham, Physical Review, 1965, **140**, A1133–A1138.
25 G. Kresse and J. Furthmüller, Physical Review B, 1996, **54**, 11169–11186.
26 J. P. Perdew, K. Burke and M. Ernzerhof, Physical Review Letters, 1996, **77**, 3865–3868.
27 A. V. Krukau, O. A. Vydrov, A. F. Izmaylov and G. E. Scuseria, The Journal of Chemical Physics, 2006, **125**, 224106.
28 P. E. Blöchl, Physical Review B, 1994, **50**, 17953–17979.
29 D. West, Y. Y. Sun, H. Wang, J. Bang and S. B. Zhang, Physical Review B, 2012, **86**, 121201.
30 C. Freysoldt, B. Grabowski, T. Hickel, J. Neugebauer, G. Kresse, A. Janotti and C. G. Van de Walle, Reviews of Modern Physics, 2014, **86**, 253–305.
31 S. Lany and A. Zunger, Modelling and Simulation in Materials Science and Engineering, 2009, **17**, 084002.
32 J. M. Adamczyk, L. C. Gomes, J. Qu, G. A. Rome, S. M. Baumann, E. Ertekin and E. S. Toberer, Chemistry of Materials, 2021, **33**, 359–369.
33 J. Qu, C. E. Porter, L. C. Gomes, J. M. Adamczyk, M. Y. Toriyama, B. R. Ortiz, E. S. Toberer and E. Ertekin, Journal of Materials Chemistry A, 2021, **9**, 26189–26201.
34 M. Y. Toriyama, J. Qu, G. J. Snyder and P. Gorai, Journal of Materials Chemistry A, 2021, **9**, 20685–20694.
35 S. Ohno, K. Imasato, S. Anand, H. Tamaki, S. D. Kang, P. Gorai, H. K. Sato, E. S. Toberer, T. Kanno and G. J. Snyder, Joule, 2018, **2**, 141–154.
36 V. Stevanović, S. Lany, X. Zhang and A. Zunger, Physical Review B, 2012, **85**, 115104.
37 C. Bellabarba, Materials Letters, 1998, **36**, 299–302.
38 J. J. Plata, V. Posligua, A. M. Márquez, J. Fernandez Sanz and R. Grau-Crespo, Chemistry of Materials, 2022.
39 A. Zevalkink, D. M. Smiadak, J. L. Blackburn, A. J. Ferguson, M. L. Chabinyc, O. Delaire, J. Wang, K. Kovnir, J. Martin, L. T. Schelhas, T. D. Sparks, S. D. Kang, M. T. Dylla, G. J. Snyder, B. R. Ortiz and E. S. Toberer, Applied Physics Reviews, 2018, **5**, 021303.
40 H. Xie, E. S. Bozin, Z. Li, M. Abeykoon, S. Banerjee, J. P. Male, G. J. Snyder, C. Wolverton, S. J. L. Billinge and M. G. Kanatzidis, Advanced Materials, 2022, **34**, 2202255.
41 Y. Zhu, B. Wei, J. Liu, N. Z. Koocher, Y. Li, L. Hu, W. He, G. Deng, W. Xu, X. Wang, J. M. Rondinelli, L.-D. Zhao, G. J. Snyder and J. Hong, Materials Today Physics, 2021, **19**, 100428.
42 B. Fernández and S. M. Wasim, physica status solidi (a), 1990, **122**, 235–242.
43 Y. Cao, X. Su, F. Meng, T. P. Bailey, J. Zhao, H. Xie, J. He, C. Uher and X. Tang, Advanced Functional Materials, 2020, **30**, 2005861.